

# Interpretation of Vibratory Pile Penetration Based on Digital Image Correlation

J. Vogelsang, G. Huber, T. Triantafyllidis and T. Bender

**Abstract** A combined interpretation of force measurements together with the evaluation of dynamic motion around the pile based on digital image correlation (DIC) is performed to identify soil deformation during vibratory pile driving in model tests. The tests are executed under water-saturated 1g-conditions. We prove the occurrence of the so-called cavitation pile driving but without the experimental evidence of the forming of a cavity under the pile tip. Using the DIC results, first attempts are made to evaluate the volumetric cyclic deformation of soil around the pile tip during the vibro-penetration. The results show an alternation of contractancy and dilatancy in proximity of the pile tip with volumetric peak-to-peak strain amplitudes up to 2 %. They indicate drained or at least partially drained conditions. Based on the test results, existing phenomenological interpretations of soil deformation due to pile penetration are reviewed.

**Keywords** Model pile · Tip resistance · Vibratory pile driving · Slow and fast vibratory pile driving · Cavitation and non-cavitation pile driving

## 1 Introduction

The penetrating pile tip is generally considered to be the principal excitation source of ground vibrations during vibratory pile driving. This is particularly true when vibro-injection piles are used. In this case, the grout material around the pile shaft acts as a lubrication layer and reduces the shear wave propagation from the pile shaft into the surrounding soil. The pile tip, however, undergoes strong impacts and transmits pressure and shear waves into the ground. These can provoke densification around the pile or in water-saturated conditions the tendency of a pore pressure build-up

---

J. Vogelsang (✉) · G. Huber · T. Triantafyllidis · T. Bender  
Institute of Soil Mechanics and Rock Mechanics,  
Karlsruhe Institute of Technology, Karlsruhe, Germany  
e-mail: Jakob.Vogelsang@kit.edu

© Springer International Publishing Switzerland 2016  
T. Triantafyllidis (ed.), *Holistic Simulation of Geotechnical  
Installation Processes*, Lecture Notes in Applied and Computational  
Mechanics 80, DOI 10.1007/978-3-319-23159-4\_2

if the soil is not too dense. In both cases, neighbouring structures can be affected by the pile installation process [13]. With regard to the prognosis of settlements of adjacent structures, the mechanisms of pile driving and especially the interaction with the surrounding soil around the pile tip have to be understood and analysed. This pertains also to numerical simulations, where only very few valuable methods exist to quantitatively investigate pile penetration processes. Notably, for pile driving in water-saturated conditions, no numerical method is available that which could be considered as validated and recommendable for practical applications [9].

Usually, for both, theoretical and practical description two basic types of pile penetration can be distinguished: cavitational (slow) and non-cavitational (fast) pile driving [2–5, 10]. The distinction relies directly on the evolution of the tip force. Slow or cavitational vibro-penetration is a term for vibratory pile driving with large displacement amplitudes. Measurements show that during phases with pile displacement upwards the contact tip force vanishes and at least for pile driving above the phreatic level, it was concluded that a cavity forms below the pile tip [2, 3, 12, 16]. The soil mechanical interpretation of this type of pile driving is that the soil below the pile tip undergoes large cyclic deformation and eventually reaches swept-out-of-memory states (SOM) [3]. As a consequence, the following penetration phase resembles a virgin loading for the soil below the pile tip and the response is very soft. Figure 1a shows the evolution of tip force during cavitational pile driving measured in high-quality in-situ tests. During non-cavitational (fast) vibro-driving the tip force does not vanish in the phase of upward motion, see Fig. 1b. In every repeated penetration phase, the soil response is very stiff and after small penetration a limit value of tip resistance is reached. The maximum tip resistance is higher than during cavitational pile driving.

Another interesting observation, especially during laboratory tests on vibratory pile driving, is the occurrence of different pile driving modes, e.g. shown in [15]. The distinction is made on the basis of the comparison of the period of characteristic motion compared to the excitation frequency. Higher modes show more complex motions and generally lower penetration rates. This topic will not be discussed in

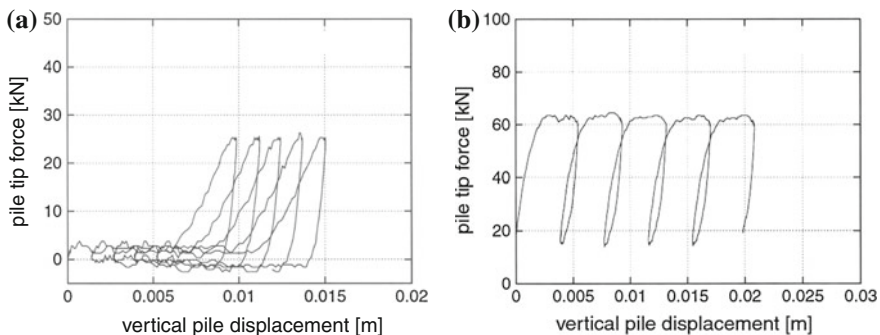


**Fig. 1** Field data of the evolution of tip force during **a** cavitational and **b** non-cavitational pile driving (from [5])

this contribution because for practical applications the simple modes are of principal interest.

Although various measurements show the described phenomena, there is still a lack of information about soil behaviour related to these. Their interpretation, e.g. provided in [3], is based on coherent and comprehensive reflections about soil behaviour in triaxial tests, but it is not validated by measurements of soil deformation during pile driving. One approach for obtaining such data are digital image correlation methods (DIC).<sup>1</sup> However, to the authors best knowledge, an application of DIC for the evaluation of cyclic soil deformation in the vicinity of a vibrating pile is not available (e.g. [11] or [19] suffer a lack of time resolution), while a great number of examples can be found for slow, monotonic pile penetration ([7, 19, 20] and many others). This can be probably attributed to the far greater effort required for the DIC investigation of cyclic, dynamic processes compared to slow processes. The camera used has to provide a frame rate of at least 10 images per vibration cycle. For typical vibration frequencies of about 30 Hz, this results in a required frame rate of 300 or more images per second, which involves substantial investment costs compared to usual digital cameras that can be used for the observation of slow processes.

## 2 Test Set-Up

The basic test set-up for the experiments presented here has already been presented in [17, 19] and is schematically illustrated in Fig. 2. The test device has a half-circular base area and an acrylic glass panel. It has been used as observation window in the symmetry plane of the pile. During the test the panel is reinforced with a steel beam attached in front to minimize deflection. Information concerning the test material and the deposition method can be found in Appendix 2.

### 2.1 Model Piles

In previous test series, as well as in many other model pile tests that can be found in the literature, piles with a rectangular cross section were used. A pile tip of this type (called pile type I) is shown in Fig. 3a, b. However, with regard to a numerical back analysis of the tests that often assume axial symmetry this pile geometry causes problems with the transferability of the results. One could argue that for comparison of forces the same base area should be used while the deformation in the observation window probably depends more on the pile geometry in this plane.

---

<sup>1</sup>The term particle image velocimetry (PIV) is considered to be more appropriate to hydromechanical applications. In the geotechnical context where groups of grains of the grain skeleton are used as markers and not individual particles the authors prefer the general term DIC. However, the evaluation procedures are usually based on the PIV-method.

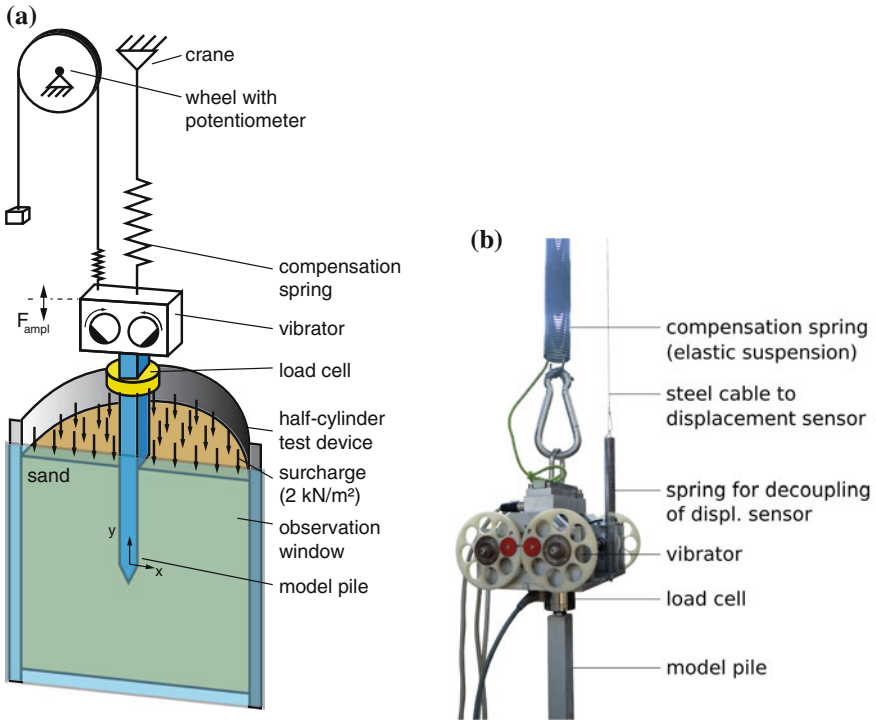


**Fig. 2** **a** Schematic test set-up and **b** detail photo of the vibrator system with connection to the pile, elastic suspension from the crane and displacement measurement

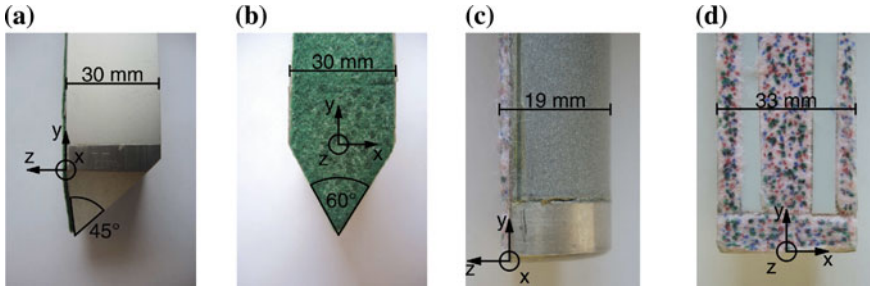
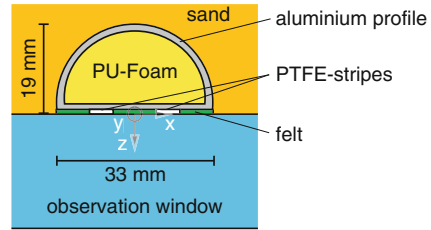


**Fig. 3** Geometry of the pile tip: **a** side view, **b** front view of pile type I and **c** side view, **d** front view of pile type II

In order to overcome these drawbacks, model piles with almost half-circular horizontal cross section (pile type II) were used in the recent tests. They are manufactured using the aluminium profiles of a cable channel system. They consist of two parts that are clipped and bonded together, installed with a head and pile tip and filled with 2-K-PU-foam. In the “symmetry plane” (contact to the observation window), two PTFE-strips ensure a stiff normal contact with the observation window and low

**Fig. 4** Schematic cross section of pile type II



friction. Around the two stripes, a layer of felt acts as a sealing against the penetration of sand grains between PTFE and window. Figure 4 shows a schematic sketch of this feature. A random pattern is painted on the felt in order to provide sufficient contrast for the evaluation of pile displacement using the DIC method (so-called seeding). The pile visible width in the “symmetry plane” ( $x$ - $y$ -plane, Fig. 2a) is 33 mm. Together with the PTFE, the width into the sand body ( $y$ - $z$ -plane) is 19 mm. Thus the cross section of pile type II is  $937.5 \text{ mm}^2$ , compared to  $855 \text{ mm}^2$  of a half-circle with 16.5 mm radius. The pile tip of type II is shown in Fig. 3c, d. A schematic cross section of this pile is given in Fig. 4.

## 2.2 Vibrator System

A small vibrator mounted on top of the model piles is used in the experiments, Fig. 2b. The vibrator has a mass of  $m_{\text{vib}} = 6734.5 \text{ g}$  and four pairwise counter-rotating eccentric masses with 37 g each. The static moment is  $0.005476 \text{ kgm}$ . The vibrator is servo controlled and the excitation frequency can be adjusted continuously in the range of 0–50 Hz. It is also possible to record the eccentric position. Using a photoelectric light barrier, the digital output signal varies between two extremes depending on whether the vertical centrifugal force is oriented downwards or upwards.

## 2.3 Instrumentation and Data Acquisition

The following instrumentation is used in recent tests:

- The force acting between vibrator and pile is measured using a load cell with 10 kN measuring range and linearity errors smaller than 0.5 % (HBM Type U2A). It has a stiffness of approximately 200 kN/mm, its natural frequency in combination with the pile is about 10 times higher than the highest vibration frequency. The load cell is connected between the bottom plate of the vibrator and the pile head.
- The global penetration is measured with a potentiometric displacement sensor connected to an impeller. A thin steel cable is fastened with a spring to the vibrator and runs over the rim of the impeller. On the other side, a counterweight of 0.4 kg

tauts the cable, see Fig. 2. The sensor is isolated from the vibrations by a spring connected in series (low-pass filtering). Using this set-up, the sensor records only the trend of displacement. The measurement range is about 1.5 m with approximate resolution of 0.25 mm.

- The eccentric position is recorded using a light barrier as described in Sect. 2.2.
- An acceleration sensor is attached to the vibrator. It is assumed that the connections and the pile are stiff enough to consider this measurement at the base of the vibrator as representative for the pile. A PCB 321 A02 acceleration sensor with a range of  $\pm 50$  g is used.
- Image data of the tests are obtained using a high-speed camera with high-resolution lens (Basler ACE acA2000-340 km). It captures up to 352 images per second with  $2040 \times 1088$  pixel resolution. The region of interest is chosen in such a way that one pixel corresponds to approx. 0.1 mm and 5 pixel to a  $d_{50}$  grain. The incremental displacements (displacements between one image and the following) are evaluated using the PIV software JPIV [14]. The utilized settings as well as information about the summation of incremental displacements and strain calculation are given in Appendix 1.

The measurements are recorded with a multichannel data acquisition system (HBM MGCplus) with simultaneous sampling and digital filtering. A sampling rate of 1200 Hz and 200 Hz low-pass Bessel filtering was used in the tests.

### 3 Test Results

We concentrate on a detailed description of cyclic soil behaviour around the vibrating pile tip on the basis of a selected section of a test with pile type II. In additional tests, similar results were obtained. The soil is considered to be nearly fully saturated and has an initial void ratio of  $e_0 = 0.691$  which corresponds to a medium density ( $I_D = 0.53$ ). The sand body has a height of 0.85 m and the pile tip is initially located 0.35 m below the sand surface. A vibration frequency of 24 Hz is used. The vibration is applied only for a few seconds. In doing so, the global penetration is kept small because the test results serve as a basis for the validation of FE simulations similar to those presented in [8] where the simulation technique is restricted to very small pile penetrations.

#### 3.1 Penetration Mode—Identification of “Cavitation” Pile Driving?

Figure 5 shows the evolution of measured pile head force plotted over the pile displacement evaluated with DIC for a selected time period. Only three characteristic cycles of pile motion are plotted. The second period of motion is highlighted with

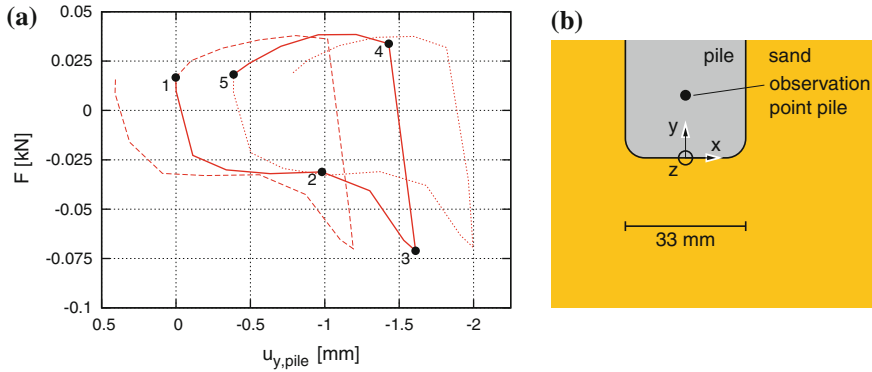


**Fig. 5** **a** Typical pile head force-displacement-curve for three selected cycles—the pile displacements are obtained from DIC analysis for a representative observation point illustrated in **(b)**

a solid line. The pile displacement is set to zero at the beginning of the highlighted cycle (highest pile position in this cycle). Important curve points are marked with numbers and referred to in the subsequent figures.

All cycles in Fig. 5 are comparable and the period of motion corresponds to the excitation period. The pile head force changes between tension and compression during each cycle and the compression force increases significantly towards the end of the downward motion between the points nr. 2 and 3. The pile penetrates with approximately 0.4 mm per cycle. The evolution of pile head force indicates cavitation pile driving. In contrast to the tip force, the head force does not vanish in the phases of upward motion because it also contains the shaft friction and inertia forces.

In Fig. 5, between the moments 1 and 2 resp. 4 and 5, distinct phases with constant force can be observed. These phases indicate that the pile tip loses contact to the soil and a small gap (cavity) forms below the tip. Therefrom the term *cavitation* pile driving [3, 4, 16] has been deduced. The tip force vanishes and the measured force at the pile head contains only inertial and shaft friction forces (and, possibly, a resulting pore pressure force for saturated soil). Considering the image data, the forming of a cavity is not evident. In order to investigate a possible opening and closure of such kind of cavity, Fig. 6 compares the pile displacements to the displacements of a material point in the soil 7.5 mm below the pile tip for the same time periods like in Fig. 5.

The zero value of the pile displacements is also used for the soil displacement to visualize the initial offset. Points closer to the pile tip cannot be evaluated reliably by DIC. Reasons therefore are the large deformations in this zone and mainly the material transition involving problems with overlapping DIC search patches.

From Fig. 6a, it can be seen that pile and soil move almost in phase in both modes. The displacement amplitudes of the pile are larger, but the evolution is very similar. The different amplitudes are at least partly contributed to a deformation of

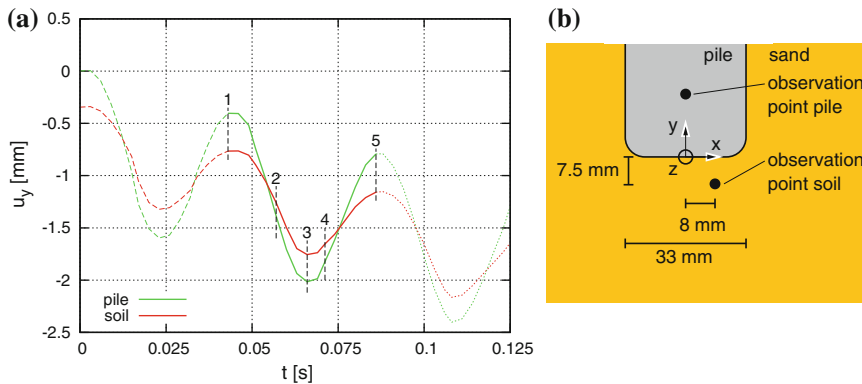


**Fig. 6** **a** Chronological evolution of displacements of the pile and a point below the pile tip for three selected cycles from DIC and **b** location of the observation points

the soil between the considered point and the pile tip. Even without this deformation the amplitude difference of about 0.35 mm cannot justify the displacement of about 1 mm necessary to mobilize tip resistance (between the moments 1 and 2 in Fig. 5). In the case of a formation of a cavity below the pile tip, one could also expect to detect the subsequent impact as a sharp bend in the displacement curve of the soil. In Fig. 6a nothing like this can be observed, the soil displacements follow the pile displacements without visible delay. The results indicate that the occurrence of a cavity is not a prerequisite of the cavitation type of pile driving in saturated soil.

## 3.2 Deformation Mechanism During Vibro-Penetration

### 3.2.1 Incremental Displacement Fields

Figure 7 shows the isolines of the incremental horizontal and vertical displacement fields obtained from the DIC analysis. The incremental displacements are separately calculated for the time periods between the characteristic curve points already marked in the preceding figures. The current pile position is indicated with thick solid line.

During the first downward phase of pile motion (from 1 to 2), the soil under the pile is pushed horizontally out- and vertically downwards, Fig. 7a. Vertical displacements dominate below the pile tip, whereas horizontal displacements occur also beside and above. The maximum horizontal displacements occur directly below the pile shoulders. The contours of vertical displacement downwards have a bubble shape of roughly one pile diameter, located centrally below the pile tip. Also laterally, above the pile shoulders, some displacements occur. The displacements are directed upwards, apart from the pile shaft and are more pronounced on the left-hand side of the pile. From 2 to 3, in the phase where tip resistance is mobilized, only under



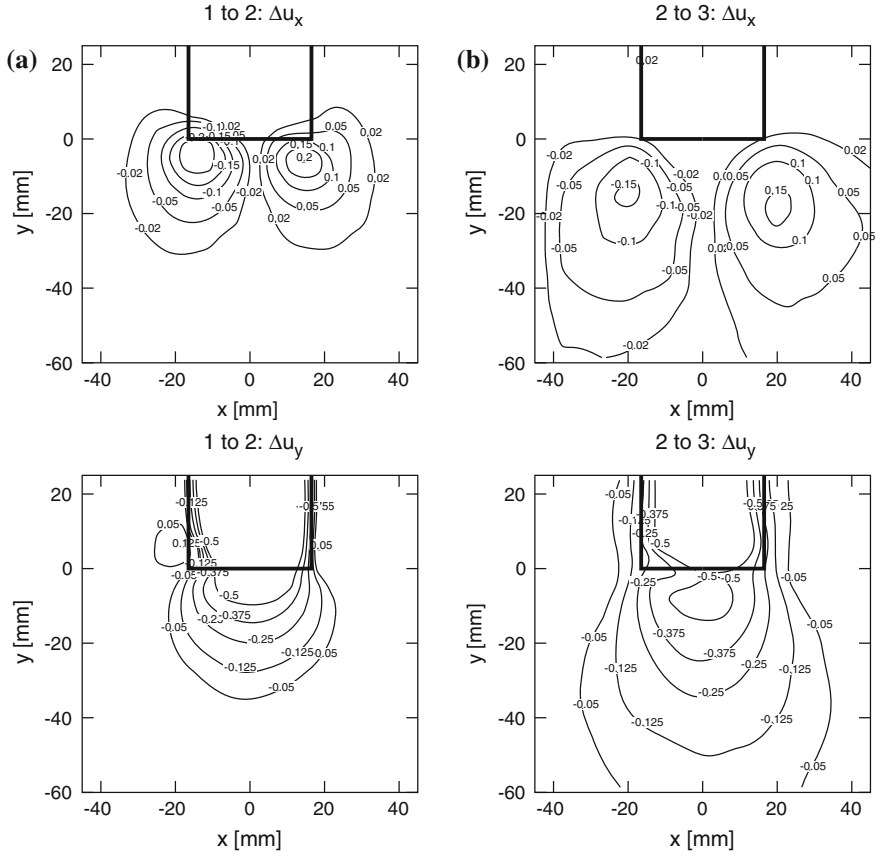


**Fig. 7** Isolines of incremental in-plane *horizontal* and *vertical* displacements  $\Delta u_x$ ,  $\Delta u_y$  (top down) in vicinity to the pile tip obtained from DIC analysis: column **a** phase 1 to 2, **b** 2 to 3 (all values in mm)

the pile tip significant displacements are observed, Fig. 7b. Compared to Fig. 7a, a larger soil zone is affected. The zone with significant displacement gradients extends approximately over twice the pile diameter into the depth. The maximum horizontal displacements are now located at about half the pile diameter under the pile shoulders. During upward pile motion, the displacements reverse, Fig. 8c, d. Both qualitatively and quantitatively, the horizontal and vertical displacements in the phase 4 to 5, Fig. 8d, resemble to the displacements in the very first phase, from 1 to 2, but with reversed sign. Compared to the phase 2 to 3, Fig. 7b, the displacements during upward pile motion concentrate on the direct vicinity of the pile tip.

Considering Figs. 7 and 8, an important result is the symmetry of the displacement field with respect to the y-axis (pile centre line) in the plane of the observation window. This symmetry is indispensable for the calculation of volumetric strain under assumption of axial symmetry (results are given below, Sect. 3.4).

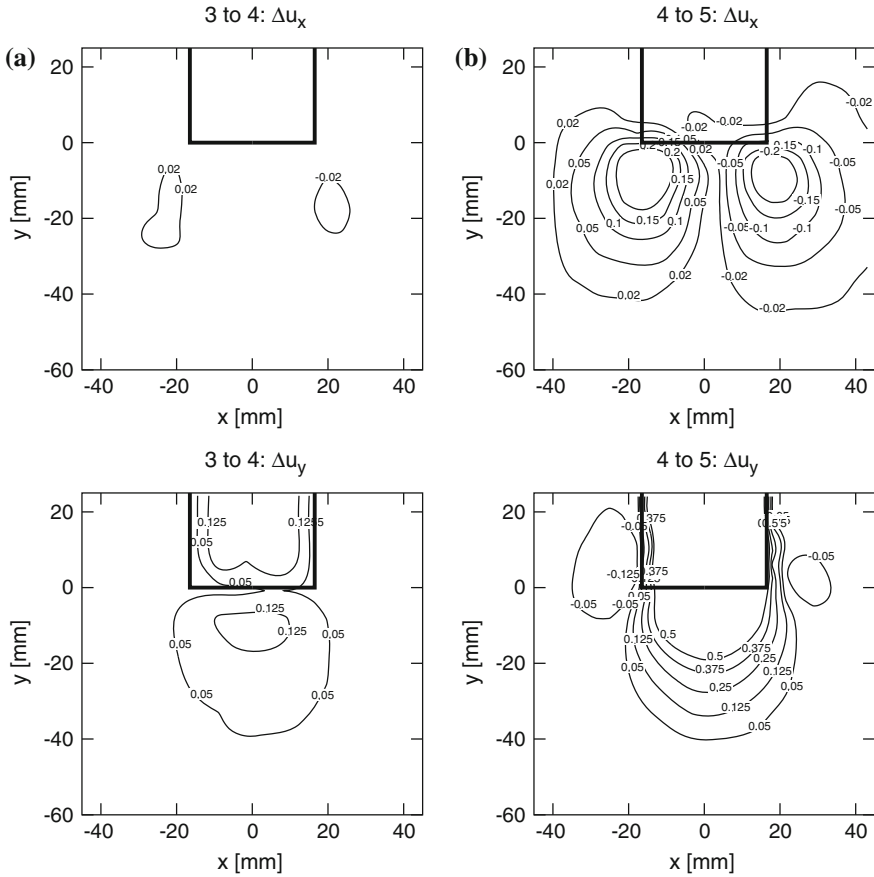


**Fig. 8** Isolines of incremental in-plane *horizontal* and *vertical* displacements  $\Delta u_x$ ,  $\Delta u_y$  (top down) in vicinity to the pile tip obtained from DIC analysis: column **c** phase 3 to 4 and **d** 4 to 5 (all values in mm)

In Figs. 7 and 8, some problems related to the DIC evaluation of pile displacements can be observed. Generally, the pile should move like a rigid body but for some phases displacement gradients can be seen along the pile contours. These problems are mainly attributed to the displacement jump at the interface pile–soil. Such discontinuity disturbs the DIC evaluation in this zone. Also overlapping search patches containing information of pile and soil can occur where usually the sand provides more contrast and determines the evaluation of a mixed patch. The evaluation in the sand should not be affected by these problems. In the literature, the pile region is often omitted. This indicates that the difficulty related to the observation of such zones is quite common.

### 3.2.2 Incremental Deformation Fields

Figures 9 and 10 show the incremental in-plane strain fields obtained from DIC analysis. Each column corresponds to one phase with horizontal, vertical and maximum shear strains  $\Delta\epsilon_{xx}$ ,  $\Delta\epsilon_{yy}$ ,  $\Delta\gamma_{\max}$  (top down). The mechanical sign convention is used (compression negative). Figure 9 contains the two phases of downward pile motion and Fig. 10 the upward pile motion.

The calculation of strain is performed basing on the incremental displacement fields (slightly smoothed using a spline method) according to the procedure described in Appendix 1.

The incremental strains occurring during the first downward phase of motion from 1 to 2 are plotted in Fig. 9a. In this phase, a bubble-shaped region is subjected to large shear deformations (greater than 4%). Vertical compression and horizontal extension are observed directly below the pile tip. On the sides below, the soil is mainly compressed in horizontal direction. Above the pile tip, horizontal and vertical compression occurs. The centre of the almost circular region around the pile tip that undergoes large shear deformation is located a few mm below the pile tip and spreads also into the zone above the pile shoulder. The consequences of this observation will be discussed later on. In the phase from 2 to 3, Fig. 9b, only below the pile tip significant deformation is observed. The extension of the deformed region is larger compared to phase 1 to 2. The deformation pattern is in accordance to other results, e.g. [19, 20]. In the short phase of upward motion from 3 to 4, only small deformations occur, Fig. 10a. In the main observation zone, vertical extension and horizontal compression below the pile tip have been measured. The shear deformation concentrates on this bubble-shaped zone. The deformations occurring in the phase 4 to 5, Fig. 10b, are similar to those in phase 1 to 2 but with reversed sign.

The problems with the evaluation of the pile, already detected in Figs. 7 and 8, are even more evident after strain calculation. However, the focus of this study lies on the soil region that provides an excellent speckle and is much better evaluated. Only a small zone of a few mm vertically below the pile tip is disturbed and cannot be interpreted. If an improved evaluation of the pile itself is desired, this could be achieved by two separate evaluations: one for the pile and one for the soil region.

### 3.3 Displacements Trajectories During Vibro-Penetration

In Fig. 11, the displacement trajectories of selected material points around the pile tip are presented. Figure 11e shows a schematic overview of the initial position of the four points with regard to the pile tip. The initial position of the pile and its current position at the beginning of the highlighted cycle (point 1) are illustrated as well. Point A is located below the pile tip while the points B, C and D are chosen slightly beside the pile at different vertical positions. Figure 11a plots the displacement trajectories together for all four points for a time period of one second after the start of the

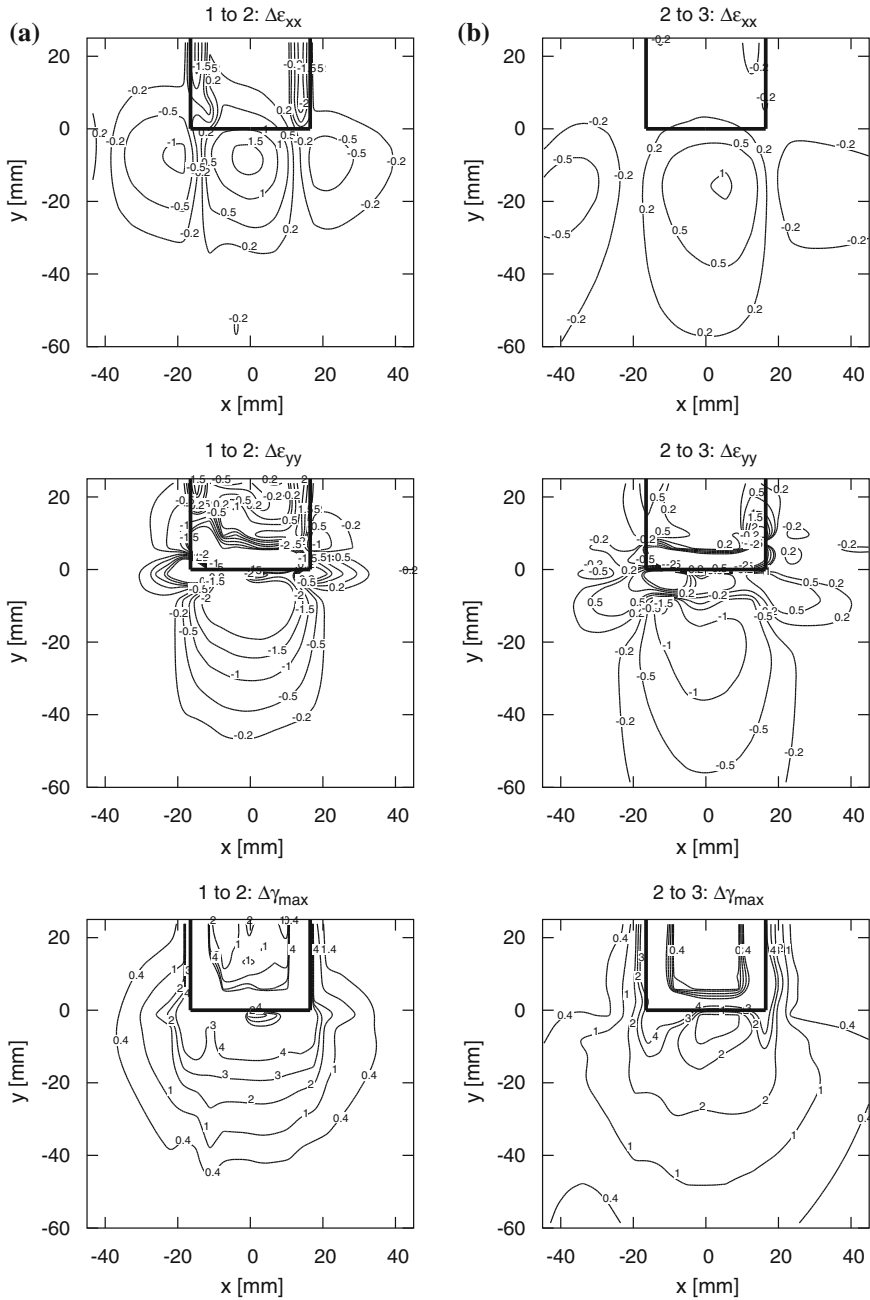


**Fig. 9** Isolines of logarithmic incremental in-plane *horizontal, vertical and maximum shear* strains  $\Delta\epsilon_{xx}$ ,  $\Delta\epsilon_{yy}$ ,  $\Delta\gamma_{\max}$  (*top down*) in vicinity to the pile tip during the downwards motion of the pile calculated on the basis of DIC results: column **a** phase 1 to 2, **b** 2 to 3 (all values in %)

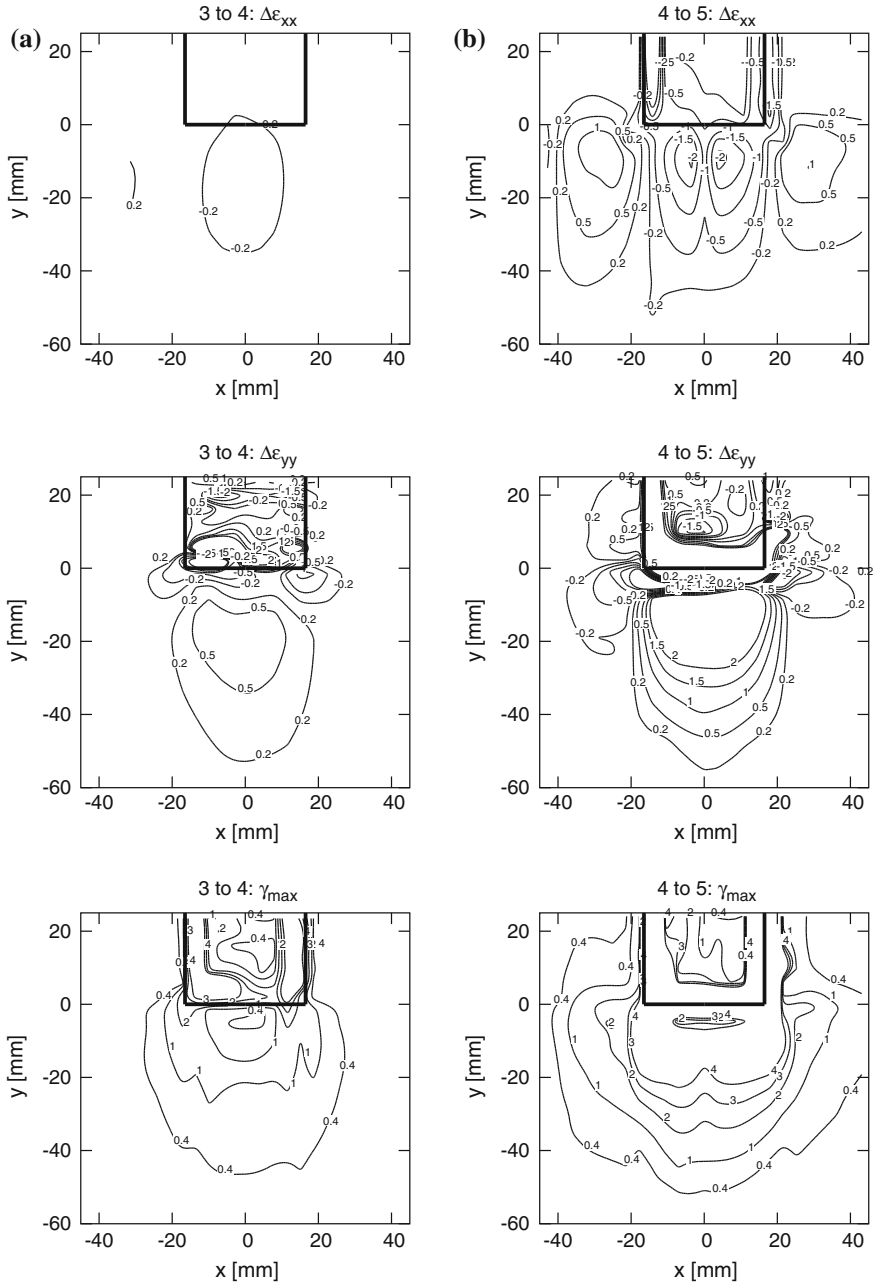


**Fig. 10** Isolines of logarithmic incremental in-plane *horizontal*, *vertical* and *maximum shear* strains  $\Delta\epsilon_{xx}$ ,  $\Delta\epsilon_{yy}$ ,  $\Delta\gamma_{\max}$  (top down) in vicinity to the pile tip during the upwards motion of the pile calculated on the basis of DIC results: column c phase 3 to 4 and d 4 to 5 (all values in %)

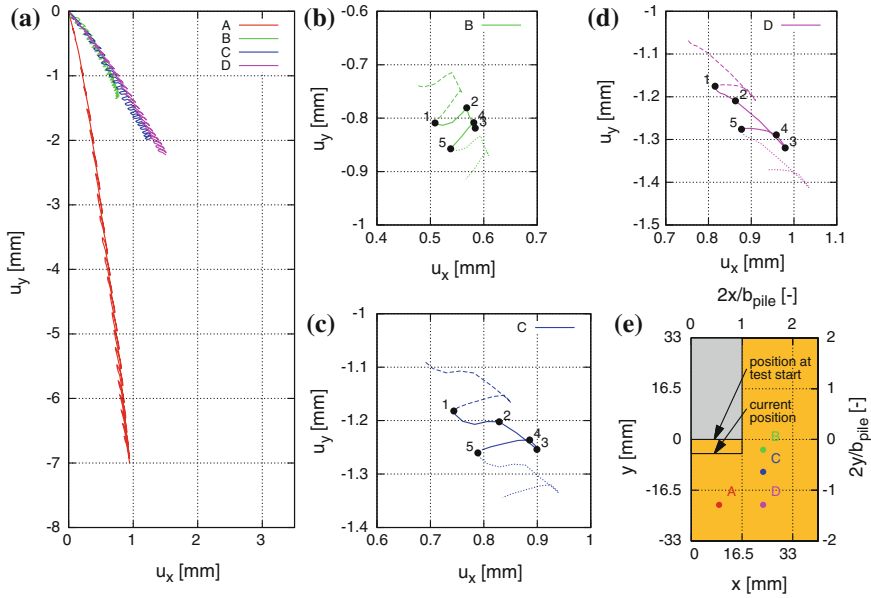


**Fig. 11** Displacement trajectories of selected points in vicinity to the pile tip: **a** overview, **b–d** individual graphs for each point during three selected cycles and **e** location of the selected points

vibration. Figure 11b–d plot the trajectories of B, C and D separately for the same time period as in Figs. 5 and 6. Although different axis ranges are used the trajectories are equally scaled in size. Point A is omitted because the point moves mainly in vertical direction and a displacement trajectory is not an appropriate visualization for such kind of displacement.

From Fig. 11a, it can be seen that the point A moves primarily in vertical direction and is pushed downwards by the pile. The other points undergo significantly smaller displacements with stronger horizontal component and larger horizontal amplitudes. They have a very similar displacement trend. Considering the evolution of cyclic displacements in Fig. 11b–d, a clear relation to the phases identified in the evolution of pile head force during each cycle can be observed. In the first downward motion phase, points nr. 1–2, the soil moves outwards, apart from the pile tip. This means a displacement upwards for point B, sideways for C and diagonally downwards for D. In the tip resistance phase, nr. 2 to 3, all points are pushed almost linearly down- and sideways. During the short-time increment from 3 to 4, the displacements reverse and the soil moves along a short section of the path followed before. Subsequently, the displacement kinks and the soil moves towards the pile tip: B and C side- and downwards and D only sideways.

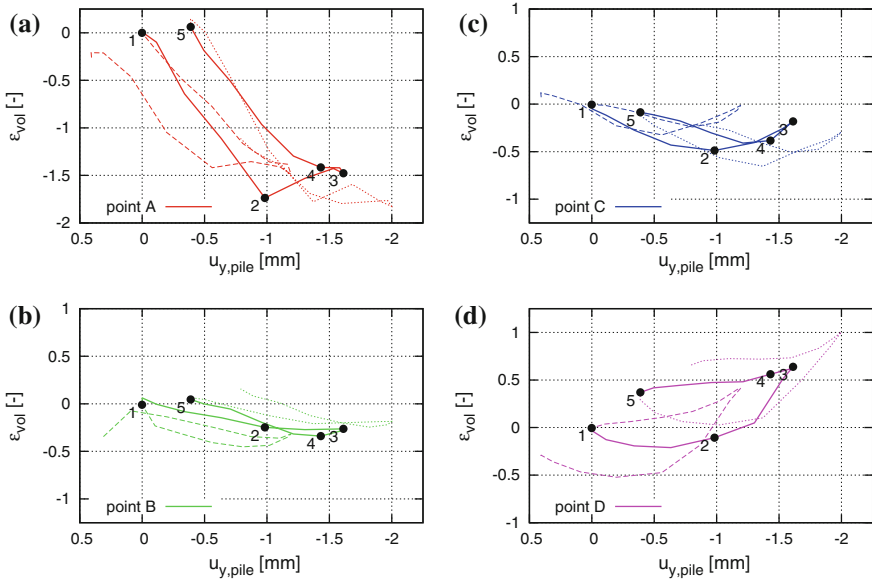


**Fig. 12** Logarithmic volumetric strain  $\varepsilon_{vol}$  calculated on the basis of DIC results assuming axial symmetry plotted versus the pile displacement  $u_{pile}$  for four points during three selected vibration cycles

### 3.4 Cyclic Volumetric Soil Behaviour During Vibro-Penetration

Figure 12 illustrates the volumetric soil deformation  $\varepsilon_{vol}$  around the pile tip exemplary for the points A–D defined in Fig. 11. Assuming axial symmetry,  $\varepsilon_{vol}$  is calculated according to the procedure given in Appendix 1. The volumetric strain is plotted over the pile displacement to visualize the connection to the force-displacement curve and to keep the points comparable. Pile displacement and volumetric strain are set to zero at the beginning of the highlighted cycle.

In all four cases, the volumetric strain oscillates considerably during every cycle, which proves at least partially drained conditions. This is an important result because it shows that a numeric code suitable for a simulation of the experiment has to deal with dynamic consolidation. The largest peak-to-peak amplitude of volumetric strain is observed for points A (1.7%). The others points show smaller amplitudes of 0.3–0.9%. Almost always a reversal of the pile motion is accompanied by a strain reversal and contractant soil behaviour. Towards the end of each downward and upward motion, the tendency to dilatancy is observed. During downward pile motion, the mobilization of dilatancy corresponds to the phases with strong increase of tip resistance (between the points 2 and 3 in Fig. 12).

## 4 Interpretation and Postulated Mechanism

During cavitational pile driving, the increase of tip resistance is slow compared to non-cavitational pile driving. The explanation given in [3] is that in the upward motion of the pile, the soil is subjected to large deformation with change of sign of the shear stress compared to the preceding penetration phase. The ratio of principal stress reverses and the horizontal stress is greater than the vertical stress. As a consequence of this, the soil response in the new penetration phase is very soft. The assumption for the phases without tip force is the opening and closure of a cavity. The time when the tip force is restarting to increase is interpreted as the moment of establishing new contact.

This explanation seems reasonable and comprehensive for pile driving in dry soil but it is found that the qualitative evolution of pile head force measured in our experiments under water-saturated conditions is very similar. As described above the opening and closure of a cavity below the pile tip is unlikely to occur in the experiments and cannot explain the long phases without tip resistance (phases 1 to 2 resp. 4 to 5). Such cavity would also stand in contrast to the fact that significant soil deformation is observed in these phases (especially in the region laterally above the pile tip). When tip resistance is mobilized (phase 2 to 3), the soil deformation concentrates on the region below the pile tip.

A possible explanation for this deformation mechanism is a type of pumping effect. When the pile performs large displacements upwards, it frees some space under the pile tip which provokes suction. The pore fluid has the tendency to fill this space and flows towards the pile tip. This creates drag forces in the soil and the grains have to follow the fluid motion. When the pile motion reverses, also the drag forces reverse and the soil is pushed radially apart by the pore fluid. During these phases, the effective stress in the soil in direct vicinity to the pile tip is very low and the soil-water mixture behaves more like a viscous fluid. The pile tip does not necessarily have effective contact with the grain skeleton. The process is very similar to the closure and expansion of a spherical cavity. Then suddenly, the grain skeleton is reformed, load transfer between pile and soil is enabled and tip resistance is mobilized. A large zone below the pile tip is sheared and can mobilize dilatancy. Necessary conditions for this mechanism are large displacement amplitudes and partially drained conditions.

## 5 Conclusions and Outlook

Vibratory pile driving was investigated using model tests in a half-cylinder-shaped test device with an observation window in the symmetry plane. The pile motion along this window was recorded using a high-speed digital camera. The pile displacements and deformation of saturated soil were evaluated by means of DIC.



Important conclusions from the experimental results are:

- The evolution of tip resistance observed in the test results presented above indicates cavitation pile driving. The characteristic points on the piles' force-displacement curve correlate with sudden changes in the directions of displacement/deformation in the soil.
- Under water, the forming of a gap or cavity is not a necessary condition for the occurrence of slow or cavitation pile driving. A sufficient pile displacement upwards and the vanishing of the tip force as a result of this seems to be a more appropriate condition. However, it is of course possible that a cavity forms below the pile under different conditions (drainage, displacement amplitude, etc.).
- On the basis of the displacement and deformation fields around the pile tip evaluated by DIC in the observation plane, the symmetry of the process with respect to a plane perpendicular to the observation plane through the centre line of the pile was confirmed. Assuming axial symmetry with respect to the centre line of the pile, the calculation of volumetric strains was performed and the occurrence of the alternation of contractant and dilatant behaviour was demonstrated.
- In the phases with negligible tip resistance—usually contributed to the opening and closure of a cavity—the pile can be in contact with the soil, but without significant effective load transfer. The deformation mechanism in these phases is similar to a spherical cavity expansion. A possible explanation is the occurrence of a pumping effect induced by the cyclic pile motion. This provokes cyclic pore fluid flow that drags and pushes the soil simultaneously to the pile motion. The increase of tip resistance coincides with a dilatant soil behaviour below the pile tip.

Important topics of future work are the direct measurements of tip resistance together with pore pressure in vicinity to the vibrating pile tip. Related to these measurements, the actual degree of saturation obtained from the sample preparation method has to be reviewed. The work presented here concentrates on the so-called cavitation pile driving. Further studies will be carried out on other types of vibratory pile driving such as non-cavitation pile driving. Using the current test set-up, a surcharge load has to be applied therefore in order to reduce the upward pile motion. Another interesting field of research is the investigation of higher vibration modes. It is of practical interest to avoid these modes, therefore the reasons for their occurrence will be studied using the approach described in this contribution.

## **Appendix 1: Summation of Incremental Displacements and Strain Calculation Procedure**

The DIC procedure evaluates a series of images and calculates the incremental displacements  $\Delta \mathbf{u}_{DIC}^{(i)}$  (displacements occurring between image  $i-1$  and  $i$ ) for a fixed grid in eulerian coordinate system. Search patches of  $32 \times 32$  pixel that are detected in zones four times as large are used for this evaluation. In order to obtain the total

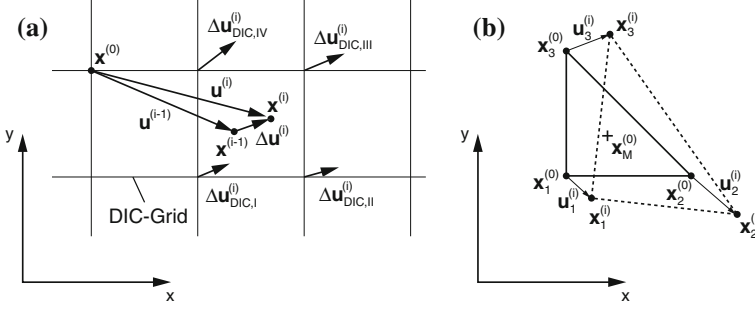


**Fig. 13** **a** Interpolation of incremental displacements  $\Delta \mathbf{u}$  from DIC results  $\Delta \mathbf{u}_{DIC}$  and summation to total displacements  $\mathbf{u}$  and **b** 3-Node element for strain calculation

displacements  $\mathbf{u}^{(i)} = \mathbf{u}(\mathbf{X}, t_i)$  with respect to a reference configuration defined in the first image, the incremental displacements have to be summed. Therefore, material points  $\mathbf{X}$  defined in the reference configuration are followed throughout the image series. Since a material point of the reference configuration lies generally not on a mesh point of the current configuration, its incremental displacement  $\Delta \mathbf{u}^{(i)}$  has to be interpolated using the information of the four surrounding points,  $\Delta \mathbf{u}_{DIC,I-IV}^{(i)}$ . Linear interpolation functions are used. The incremental displacements  $\Delta \mathbf{u}^{(i)}$  are then added to the total displacement of the preceding step to obtain the current total displacement  $\mathbf{u}^{(i)}$ . This procedure is illustrated in Fig. 13a.

Similar to [20], for strain calculation a triangular 3-node element with linear interpolation functions is used, Fig. 13b.

For this element the deformation gradient  $\mathbf{F}$  is calculated as the derivative of the current position  $\mathbf{x}^{(i)} = [x^{(i)}, y^{(i)}]^T$  with regard to the reference configuration  $\mathbf{X} = \mathbf{x}^{(0)} = [X, Y]^T$ . Linear interpolation functions  $N_j$  are used for the approximation of the current configuration.

$$\mathbf{F} = \frac{\partial \mathbf{x}^{(i)}}{\partial \mathbf{X}} = \sum_{j=1}^3 \frac{\partial N_j}{\partial \mathbf{X}} \mathbf{x}_j^{(i)} \quad (1)$$

The derivatives of the interpolation functions can be calculated from the nodal coordinates in the reference configuration:

$$\frac{\partial N_1}{\partial X} = \frac{1}{2A_e}(Y_2 - Y_3); \quad \frac{\partial N_1}{\partial Y} = \frac{1}{2A_e}(X_3 - X_2) \quad (2)$$

$$\frac{\partial N_2}{\partial X} = \frac{1}{2A_e}(Y_3 - Y_1); \quad \frac{\partial N_2}{\partial Y} = \frac{1}{2A_e}(X_1 - X_3) \quad (3)$$

$$\frac{\partial N_3}{\partial X} = \frac{1}{2A_e}(Y_1 - Y_2); \quad \frac{\partial N_3}{\partial Y} = \frac{1}{2A_e}(X_2 - X_1) \quad (4)$$

With the element area  $A_e$ :

$$A_e = 1/2[X_1(Y_2 - Y_3) + X_2(Y_3 - Y_1) + X_3(Y_1 - Y_2)] \quad (5)$$

The Right Cauchy-Green-deformation tensor  $\mathbf{U}$  is obtained as follows:

$$\mathbf{U} = (\mathbf{F}^T \cdot \mathbf{F})^{1/2} \quad (6)$$

The principal in-plane (Hencky-)strains and the maximum in-plane shear strain are obtained from the eigenvalues  $U_{I/II}$  of  $\mathbf{U}$ . Therefrom, the volumetric strain  $\varepsilon_{\text{vol}}$  is calculated assuming axial symmetry ( $u_x \hat{=} u_r$ ).

$$\varepsilon_I = \ln U_I; \quad \varepsilon_{II} = \ln U_{II}; \quad (7)$$

$$\gamma_{\text{max}} = \varepsilon_I - \varepsilon_{II}; \quad \varepsilon_{\text{vol}} = \varepsilon_I + \varepsilon_{II} + \ln(1 + u_x/X) \quad (8)$$

## Appendix 2: Test Sand, Deposition Method and Uniformity Control

A poorly graded medium quartz sand with sub-rounded grains is used in the tests. A typical grain size distribution and some granulometric properties are given in Fig. 14a. The minimum and maximum void ratios at negligible stress level are  $e_{\text{min}} = 0.549$  and  $e_{\text{max}} = 0.851$ . From permeability tests with constant head, the dependence of the coefficient of permeability  $k$  on the porosity  $n$  was evaluated. Results are given in

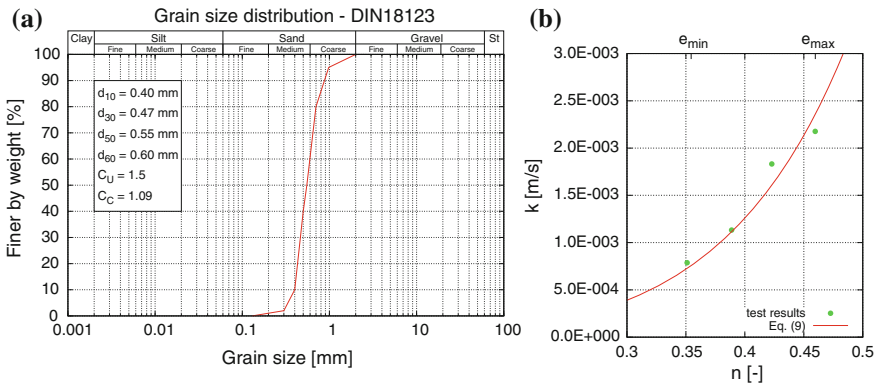


**Fig. 14** **a** Grain size distribution of the test sand (Karlsruhe Sand) and **b** results of permeability tests with constant head for different porosities

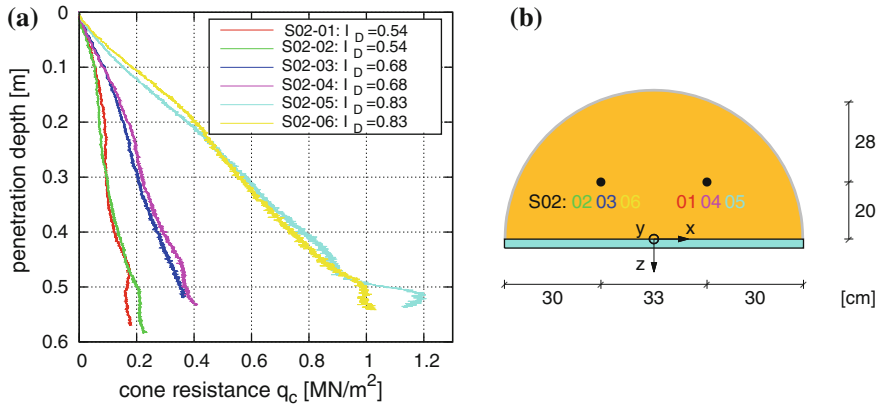


**Fig. 15** CPT for uniformity control: **a** measurements and **b** position of the CPTs

Fig. 14b. For a rough estimation of the permeability  $k$  as a function of the porosity  $n$ , the well-known Kozeny/Carman-equation [1, 6] was fitted to the test results, Eq. 9:

$$k(n) = \frac{1}{308} \cdot \frac{\gamma_w}{\eta_w} \cdot \frac{n^3}{(1-n)^2} \cdot d_w^2 \quad (9)$$

with the specific weight of water  $\gamma_w = 10 \text{ kN/m}^3$ , the dynamic viscosity of water  $\eta_w = 1.137 \times 10^{-3} \text{ kNs/m}^2$  and the effective grain size  $d_w = 0.5 \text{ mm}$ .

For the preparation of the vibratory pile driving tests, the model pile is fixed in the starting position and approximately half of the test device is filled with deaired water. The dry sand is pluviated onto the water surface using a travelling diffusor which is manually operated in such a way that the sand sediments in horizontal layers. This procedure results in relative densities of about 40 %. Higher densities are achieved by dynamic excitation of the test device, e.g. by applying multiple hammer blows against the base.

For numerical simulation of the tests it is essential to obtain a homogeneous density distribution. In order to control the uniformity of the sample after the described deposition and densification method a series of cone penetration tests (CPT) was conducted. The same set-up like in [18] was used. The results are shown in Fig. 15a and the position of the CPTs in Fig. 15. The same sample was used for all six CPTs. The sample was densified step-wise and after each densification two opposited CPTs with respect to the symmetry plane  $y$ - $z$  were performed. As expected, the cone resistance  $q_c$  increases for higher relative densities. The three CPT-pairs show very similar results although one could expect that the second CPT for each density is influenced by the preceding. The results indicate that the preparation method provides homogeneous samples and can be used for benchmark experiments.

## References

1. Carman, P.C.: Permeability of saturated sands, soils and clays. *J. Agric. Sci.* **29**, 263–273 (1937)
2. Cudmani, R.O., Huber, G., Gudehus, G.: Zyklische und dynamische Penetration nichtbindiger Böden, Contribution to Workshop “Boden unter fast zyklischer Belastung”, Bochum (2000)
3. Cudmani, R.O.: Statische, alternierende und dynamische Penetration in nichtbindigen Böden. Diss., Publications of the Institute of Soil Mechanics and Rock Mechanics, University of Karlsruhe, vol. 152 (2001)
4. Dierssen, G.: Ein bodenmechanisches Modell zur Beschreibung des Vibrationsrammens in körnigen Böden. Diss., Publications of the Institute of Soil Mechanics and Rock Mechanics, University of Karlsruhe, vol. 124 (1994)
5. Huber, G.: Vibrationsrammen: Großmaßstäbliche Versuche. Contribution to the Workshop “Vibrationsrammen”, Karlsruhe (1997)
6. Kozeny, J.: Ueber kapillare Leitung des Wassers im Boden. Sitzungsbericht Akademie der Wissenschaften, Wien **136**(2a), 271–306 (1927)
7. Ni, Q., Hird, C.C., Guymer, I.: Physical modelling of pile penetration in clay using transparent soil and particle image velocimetry. *Gotechnique* **60**(2), 121–132 (2009)
8. Osinov, V.A., Chrisopoulos, St., Triantafyllidis, Th.: Numerical study of the deformation of saturated soil in the vicinity of a vibrating pile. *Acta Geotech.* (2012). doi:[10.1007/s11440-012-0190-7](https://doi.org/10.1007/s11440-012-0190-7)
9. Osinov, V.A.: Numerical modelling of the effective-stress evolution in saturated soil around a vibrating pile toe. In: Triantafyllidis, Th. (ed.) *Holistic Simulation of Geotechnical Installation Processes—Numerical and Physical Modelling*, pp. 138–154. Springer, Heidelberg (2015)
10. Rodger, A.A., Littlejohn, G.: A study of vibratory pile driving in granular soils. *Gotechnique* **30**(3), 269–293 (1980)
11. Savidis, S.A., Aubram, D., Rackwitz, F.: Vibro-Injection pile installation in sand: Part II—Numerical and experimental investigation. In: Triantafyllidis, Th. (ed.) *Holistic Simulation of Geotechnical Installation Processes—Numerical and Physical Modelling*, pp. 103–131. Springer, Heidelberg (2015)
12. Schönit, M.: Online-Abschätzung der Rammguttragfähigkeit beim langsamen Vibrationsrammen in nichtbindigen Böden. Diss., Publications of the Institute for Technology and Management in Construction, University of Karlsruhe (2009)
13. Triantafyllidis, Th.: Neue Erkenntnisse aus Messungen an tiefen Baugruben am Potsdamer Platz in Berlin, *Bautechnik*, 75. Heft **3**, 133–154 (1998)
14. Vennemann, P.: JPIV-software package for Particle Image Velocimetry (2007). <http://www.jpiv.vennemann-online.de>
15. Vielsack, P., Storz, M.: Dynamics of vibratory pile driving. Workshop “Vibrationsrammen”, pp. 3–12, Karlsruhe (1997)
16. Viking, K.: The vibratory pile installation technique. *TRANSVIB 2006*, Gonin, Holeyman et Rocher-Lacoste (ed.), Editions du LCPC, pp. 65–82, Paris (2006)
17. Vogelsang, J., Chrisopoulos, S.: Experimentelle und numerische Untersuchungen zum Vibrationsrammen in nichtbindigem Boden. Beitrag zur Spezialsitzung “Forum für junge Geotechnik-Ingenieure”, 33. Baugrundtagung in Berlin (2014)
18. Vogelsang, J., Zachert, H., Huber, G., Triantafyllidis, Th.: Effects of soil deposition on the initial stress state in model tests: Experimental results and FE simulation. In: Triantafyllidis, Th. (ed.) *Holistic Simulation of Geotechnical Installation Processes—Numerical and Physical Modelling*, pp. 1–21. Springer, Heidelberg (2015)
19. Vogelsang, J., Huber, G., Triantafyllidis, Th.: On soil deformation and stress redistribution around pressed-in and vibrated displacement pile tips. In: Triantafyllidis, Th. (ed.) *Holistic Simulation of Geotechnical Installation Processes—Numerical and Physical Modelling*, pp. 44–59. Springer, Heidelberg (2015)
20. White, D.J., Bolton, M.D.: Displacement and strain paths during plane-strain model pile installation in sand. *Gotechnique* **54**(6), 375–397 (2004)

Holistic Simulation of Geotechnical Installation  
Processes

Benchmarks and Simulations

Triantafyllidis, T. (Ed.)

2016, VIII, 253 p., Hardcover

ISBN: 978-3-319-23158-7